Frontiers in Heat and Mass Transfer

Tech Science Press

https://doi.org/10.32604/fhmt.2026.079777

ARTICLE

Numerical Investigation on the Heat and Mass Transfer Characteristics of Direct Contact Condensation in a Water-Driven Steam Ejector

Da Fang[1], Xianbing Chen[2,*], Chenxiao Chu[3,*], Xinhou Liu[4], Mengyu Zhu[5] and Jinliang Zhu[6]

[1]Jinan City Planning and Design Institute, Jinan, China
[2]School of Thermal Engineering, Shandong Jianzhu University, Jinan, China
[3]Jinan Vocational College, Jinan, China
[4]Jinan Public Service Center for Small and Medium-Sized Enterprises, Jinan, China
[5]University of Jinan, Jinan, China
[6]Weifang University, Weifang, China

*Corresponding Authors: Xianbing Chen. Email: chenxianbing20@sdjzu.edu.cn; Chenxiao Chu. Email: chuchenxiao@outlook.com

Received: 28 January 2026; Accepted: 03 April 2026; Published: 29 June 2026

ABSTRACT: A three-dimensional numerical model of a water-driven steam ejector was developed using the Euler-Euler two-fluid framework. A direct-contact condensation (DCC) heat and mass transfer model was employed to simulate the complex two-phase flow and energy exchange. The distributions of gas-liquid phases, pressure, and temperature were obtained to evaluate performance. Results indicate that within the investigated operating range (p_p = 140–160 kPa), the entrainment ratio (ER) and temperature rise (DT) are highly coupled, with DT varying from 5.33 to 11.49 K. The maximum temperature rise of 11.49 K was achieved at p_p = 140 kPa, T_p = 310 K, p_s = 100 kPa, and p_b = 92 kPa. It was found that a distinct pressure jump occurs at the throat, where the entrained steam is completely condensed, followed by rapid pressure recovery in the diffuser. The steam plume length and condensation zone are strongly governed by back pressure (p_b); Increasing p_b from 92 to 114 kPa leads to a continuous reduction in ER and shifts the peak condensation zone upstream. Furthermore, the study reveals that elevated back pressure suppresses steam entrainment and shortens the condensation length, eventually leading to flow reversal when a critical p_b is exceeded. This work provides detailed physical insight into DCC mechanisms and offers quantitative references for the design of ejector-assisted components in advanced energy systems.

KEYWORDS: Steam ejector; water-driven; two phase flow; heat and mass transfer; entrainment ratio

1 Introduction

Steam ejectors have been widely applied in refrigeration [1], desalination [2,3], vacuum generation, and energy recovery systems [4,5] because of their simple structure, high reliability, and absence of moving parts [6,7]. Water-driven steam ejectors have emerged as a critical technology for low-grade thermal energy utilization and waste heat recovery systems [5,8]. These systems operate by utilizing high-pressure liquid water as the primary fluid to entrain low-pressure steam, creating a complex two-phase flow environment that dictates the device's efficiency. In this context, the Direct Contact Condensation (DCC) between the high-velocity liquid jet and the entrained vapor stream serves as the primary driver for momentum transfer and pressure recovery. While this two-phase interaction facilitates superior thermal exchange, it concurrently triggers non-equilibrium phase-change effects and flow instabilities. These phenomena can significantly degrade the entrainment ratio and overall stability if the phase-change rate and pressure distribution are not precisely controlled.

To quantify these two-phase effects, the performance of the ejector is traditionally evaluated via the entrainment ratio (ER) and the mixed-flow temperature rise. The ER serves as a direct indicator of the suction capability governed by momentum exchange, while the temperature rise reflects the intensity of the direct-contact heat and mass transfer between the liquid and vapor phases. Although prior studies [9,10] have established that operating parameters-such as primary fluid pressure and back pressure-significantly dictate these metrics, the underlying mechanism of how these parameters modulate the internal two-phase flow structure and phase-change stability remains insufficiently understood. This gap in knowledge limits the further optimization of ejector efficiency under varying industrial conditions, necessitating a more systematic investigation of the coupling between operating conditions and two-phase flow dynamics.

Experimental studies have been conducted to evaluate the performance of liquid-driven or steam ejectors under various operating conditions [4,5,10–12]. These studies provided valuable data on global performance indicators, such as ER and pressure recovery [13]. However, due to the harsh operating environment and the complex multiphase flow inside the ejector, experimental measurements are often limited to inlet and outlet conditions. Detailed information regarding gas-liquid phase distribution, local temperature evolution, pressure variation, and DCC behavior inside the ejector remains difficult to obtain experimentally.

Computational fluid dynamics (CFD) has emerged as an effective tool to overcome experimental limitations and provide detailed insight into internal flow and heat transfer characteristics [14,15]. Early numerical studies on steam ejectors mainly adopted single-phase or homogeneous equilibrium models to simplify the multiphase flow problem [16]. Although such approaches can predict overall trends, they are often inadequate for capturing interphase momentum, heat, and mass transfer, especially in systems dominated by DCC [17,18].

To improve modeling accuracy, multiphase flow models based on the Euler-Euler two-fluid framework have been increasingly applied to ejector simulations [19–21]. When coupled with appropriate DCC models, the Euler–Euler approach enables a more realistic description of phase interactions and condensation heat transfer [22,23]. Shah et al. [20] and Gulawani et al. [19] have incorporated thermal equilibrium assumptions into DCC models to enhance numerical stability and reduce computational cost, while still achieving acceptable agreement with experimental results. Four typical steam plume morphologies were identified by Zhou et al. [21], and their formation mechanisms were elucidated by analyzing void fraction and axial thermodynamic parameters in conjunction with expansion-compression wave theory. Zhang et al. [24] investigated the effect of non-condensable gas on the performance of a gas-centered water ejector, showing that a small amount of air initially enhances the ejected water flow rate, whereas higher concentrations reduce it. Xu et al. [25] reported that increasing the nozzle inlet steam pressure from 150 to 450 kPa caused the steam plume to transition from a contraction cone to an expansion-contraction structure, with a linear increase in plume length, a decreasing volumetric condensation heat transfer coefficient. Ke et al. [26] proposed a modified calculation method for a centered water nozzle steam-water ejector, successfully predicting ejector performance and shock-wave behavior under varying inlet pressures and back pressures. Zhou et al. [27] proposed a dual-ejector flat-evaporator loop heat pipe with a pressurized bi-porous wick, enhancing capillary force, reducing vapor pressure and thermal resistance, and significantly increasing maximum heat load and flux. Despite these significant advancements, a critical gap persists in the existing literature: most studies focus on isolated operating parameters or specific nozzle geometries, leaving the synergistic effects of coupled inlet and outlet conditions on both entrainment and thermal performance insufficiently explored. Furthermore, the physical mechanism by which outlet back pressure induces flow reversal has not been fully clarified within a unified multiphase framework.

In response to these research gaps, this study develops a comprehensive three-dimensional numerical model based on the Euler-Euler framework coupled with a thermal-equilibrium-based DCC model.

The novelty of this work, which distinguishes it from previous research, lies in three key aspects: Primarily, it provides a systematic analysis of the combined influence of four critical operating parameters (primary water pressure and temperature, entrained steam pressure, and back pressure), offering a more holistic performance map than prior single-variable studies. Furthermore, it specifically elucidates the internal flow physics governing the transition to flow reversal, identifying the thermodynamic triggers that disrupt the suction effect under high back pressure. Additionally, by correlating spatial gas-liquid interface evolution with macro-scale performance, this study establishes a direct link between internal condensation efficiency and overall entrainment capability. The primary objective is to provide both deeper physical insights into the governing mechanisms and practical design references for the optimization of high-efficiency water-driven steam ejector systems.

2 Numerical Methodology

To address the aforementioned research gaps-specifically the scarcity of high-fidelity internal flow data and the unresolved mechanisms of flow reversal-this section delineates the numerical framework developed to simulate the water-driven steam ejector. The ejector investigated in this study consists of several critical components: a primary water nozzle, a suction chamber, a mixing section (throat), and a diffuser. The primary high-pressure liquid water is discharged through the nozzle, creating a high-velocity jet that induces a low-pressure region in the suction chamber to entrain the low-pressure steam.

The complexity of this process lies in the intensive DCC and momentum exchange occurring at the gas-liquid interface. To capture these phenomena, which are often invisible in experimental setups, a three-dimensional multiphase model is required. By establishing this physical context, the subsequent numerical formulations are designed to specifically target the spatial evolution of phase distributions and the thermal triggers of performance degradation mentioned previously. To rigorously represent the complex phase interactions and heat transfer mechanisms involved, the following governing equations are established based on the Euler-Euler two-fluid framework.

2.1 Euler–Euler Two-Fluid Model

To accurately capture the complex non-equilibrium interfacial phenomena-specifically the intricate interphase momentum, mass, and heat transfer-occurring within the water-driven steam ejector, a comprehensive Euler-Euler two-fluid framework was implemented. The fundamental principle of this approach is to treat the liquid water and steam phases as interpenetrating continua. Unlike simplified mixture models, the Euler-Euler methodology assumes that both phases coexist at every point in the computational domain, with their respective presence quantified by the local volume fraction. A primary feature of this model is its ability to solve a separate set of conservation equations for each phase, allowing for the resolution of distinct velocity and temperature fields. This is particularly crucial in two-phase ejector simulations where significant velocity slips and thermal lags exist between the high-speed steam and the secondary water flow. The coupling between the two phases is achieved through pressure and specialized interphase exchange terms. Water was treated as the primary phase w and steam as the secondary phase v. The governing equations for the conservation of volume fraction equation, mass, momentum, and energy for phase v are formulated as follows:

$$V_v = \int_V \varphi_v \, dV, \tag{1}$$

$$\sum_{q=1}^{n} \varphi_v = 1, \tag{2}$$

$$\frac{\partial}{\partial t}\left(\varphi_v \rho_v\right)+\nabla\left(\varphi_v \rho_v \vec{v}_v\right)=\sum_{w=1}^{n}\left(m_{wv}-m_{wv}\right)+S_v, \tag{3}$$

$$\nabla\left(\varphi_v \rho_v \vec{v}_v\right)=-\varphi_v \nabla P+\nabla \tau_v+\varphi_v \rho_v g+\sum_{\rho=1}^{n}\left(R_{wv}+m_{wv}\vec{v}_{wv}-m_{vw}\vec{v}_{vw}\right)+\vec{F}_v+\vec{F}_{\mathrm{li}ft,v}+\vec{F}_{vm,v}, \tag{4}$$

$$\frac{\partial}{\partial t}\left(\varphi_v \rho_v h_v\right)+\nabla\left(\alpha_v \rho_v \vec{v}_v h_v\right)=-\varphi_v \frac{\partial P_v}{\partial t}+\nabla \tau_v+\nabla \vec{v}_v-\nabla q_v+S_v+\sum_{\rho=1}^{n}\left(Q_{wv}+m_{wv}h_{wv}-m_{vw}h_{vw}\right), \tag{5}$$

where V_v, φ_v, ρ_v, v_v, S_v, τ_v and h_v denote the total volume, volume fraction, density, velocity, mass source term, shear stress, and enthalpy of phase v, respectively. The terms m_{wv}, h_{wv}, R_{wv}, q_v and Q_{wv} represent the interfacial mass transfer, interfacial energy transfer, interfacial momentum transfer, and heat flux, respectively. The terms Q_{wv} and S_v represent the interfacial energy transfer and the interfacial mass source, respectively. To accurately capture the phase change process within the ejector, these terms are calculated based on the thermal phase change model. Detailed formulations and the specific calculation procedures for Q_{wv} *and* S_v are provided in Section 2.2 (see Eq. (14)). The interphase momentum exchange is further characterized by several hydrodynamic forces. The external body force, F_v, primarily accounts for the gravitational effect already incorporated in the momentum conservation. To capture the lateral migration of the dispersed phase within the non-uniform velocity field of the ejector, the lift force $F_{lift,v}$ is included. Additionally, the virtual mass force $F_{vm,v}$ is employed to represent the inertia exerted by the surrounding fluid during the acceleration of the dispersed phase.

2.2 DCC Model

Based on the above Eulerian framework, a condensation model derived from the thermal equilibrium principle was adopted in the numerical simulations. The condensation model is established under the following assumptions:

(1) Steam condensation occurs only at the gas-liquid interface, and no atomization of steam is considered. The interface temperature is assumed to be equal to the local saturation temperature T_{sat} corresponding to the local pressure p.

$$T_{sat}=3826.36/\left(9.3876-\ln\left(p/1000\right)\right)+45.47 \tag{6}$$

(2) The difference in sensible heat transfer across the gas-liquid interface is attributed entirely to the latent heat released by condensation.

(3) Steam is treated as the secondary phase, and steam condensation is assumed to occur in the form of condensation of numerous small spherical steam bubbles, which is consistent with the fundamental assumptions of the Euler-Euler model.

In the Eulerian framework, the steam bubble diameter d_v is used to calculate the drag coefficient. In the DCC model, it is further employed to evaluate the Reynolds number and Nusselt number. The bubble diameter is assumed to be a function of the subcooling degree [28],

$$d_v=\frac{3}{2000}-\frac{T_{sat}-T_w}{10000}. \tag{7}$$

Under the spherical bubble assumption, the interfacial heat transfer area per unit volume can be expressed as,

$$A_{vw}=6\varphi_v/d_v, \tag{8}$$

where the subscripts w and v denote water and steam, respectively. The Nusselt number, Reynolds number, and Prandtl number of the steam bubbles are defined as follows,

$$Nu_w = \frac{h_w d_v}{k_w}, \tag{9}$$

$$Re = \frac{\rho_w \left(u_v - u_w\right) d_v}{\mu_w}, \tag{10}$$

$$Pr = \frac{c_{pw} \mu_w}{k_w}, \tag{11}$$

where h_w and k_w denote the convective heat transfer coefficient and the thermal conductivity of the water phase, respectively.

The convective heat transfer coefficient on the water side, h_w, is derived from the Nusselt number. According to the correlation proposed by Hughmark [29], Nu_w is defined as:

$$Nu_w = \begin{cases} 2.0 + 0.6 Re^{0.5} Pr^{0.33}, & 0 \le Re < 776, \quad 0 \le Pr < 250 \\ 2.0 + 0.27 Re^{0.62} Pr^{0.33}, & 776 \le Re, \quad 0 \le Pr < 250 \end{cases}. \tag{12}$$

The convective heat transfer coefficient on the steam side is much larger than that on the liquid side. As long as this coefficient is sufficiently large, it has a negligible influence on the numerical results. Therefore, it is treated as a constant in the present study,

$$h_v = 10\,\mathrm{kW}/\left(\mathrm{m}^2 \cdot \mathrm{K}\right). \tag{13}$$

According to the thermal equilibrium assumption, the heat transfer rates on the gas and liquid sides are equal. The difference in sensible heat transfer across the gas-liquid interface is thus attributed to the latent heat released during condensation. Consequently, the steam condensation rate per unit volume per unit time can be expressed as,

$$m_{vw} = \frac{\left[h_w \left(T_{sat} - T_w\right) + h_v \left(T_{sat} - T_v\right)\right] A_{vw}}{H_{vw}}, \tag{14}$$

where H_{vw} denotes the latent heat of vaporization of water at the local pressure.

To implement the DCC model described above, a User-Defined Function (UDF) was developed and compiled into the ANSYS Fluent solver [30]. Since the standard Eulerian multiphase model lacks built-in correlations for subcooling-dependent bubble diameters and the Hughmark heat transfer coefficient, the DEFINE_MASS_TRANSFER macro was utilized to define the interphase mass transfer rate. The UDF execution logic at each computational cell and iteration is as follows:

(1) Variable Retrieval: The local pressure (P), phase temperatures (T_w, T_v), and phase velocities (v_w, v_v), are retrieved from the solver.

(2) Dynamic Property Calculation: The saturation temperature T_{sat} is updated based on the local pressure. The subcooling degree is then determined to calculate the dynamic bubble diameter using Eq. (6).

(3) Dimensionless Correlation: The Reynolds, Prandtl, and Nusselt numbers are computed to evaluate the liquid-side convective heat transfer coefficient via the Hughmark correlation Eq. (11).

(4) Source Term Coupling: Finally, the volumetric condensation rate m_{wv} is calculated based on the thermal equilibrium principle Eq. (13) and returned to the solver.

The mass source term is automatically incorporated into the continuity equations of both phases, while the associated latent heat is coupled to the energy equation, ensuring rigorous mass and energy conservation throughout the simulation.

2.3 Simulation Domain and Solver Settings

The comprehensive design of the water-driven steam ejector follows a coordinated multi-component approach to optimize the momentum exchange between the liquid and vapor phases. The primary water nozzle is dimensioned to deliver a high-momentum liquid jet based on the required motive power, while the geometry of the mixing chamber, throat, and diffuser is specifically tailored to facilitate the DCC process and ensure efficient pressure recovery. As illustrated in Fig. 1a, the ejector operates with the primary flow of water introduced at the center and the secondary flow of saturated steam entering circumferentially. High-pressure water jet entrains low-pressure steam in the mixing chamber, where condensation occurs, raising the water temperature; the mixture then passes through the throat and diffuser to overcome the ejector back pressure. As shown in Fig. 1b, the computational domain of the ejector was discretized using a structured hexahedral mesh to ensure superior numerical stability and convergence. The mesh was specifically refined in high-gradient areas, including the primary nozzle outlet and the mixing zone, to accurately resolve the shear layer and phase interactions. Maintaining a mesh quality higher than 0.75, the grid configuration provides a robust foundation for calculation stability and minimize numerical diffusion.

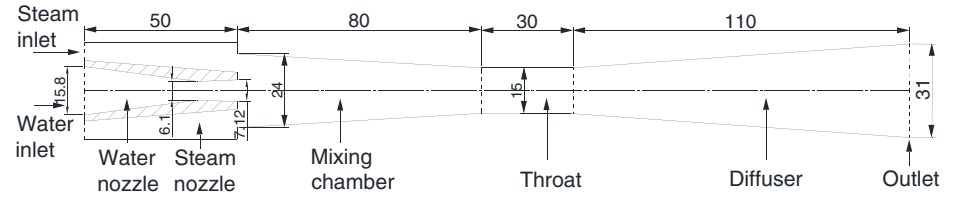

(a)

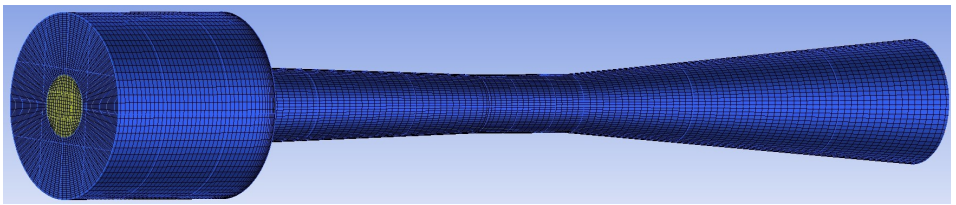

(b)

Figure 1: Schematic diagram and computational mesh of the ejector. (**a**) Schematic and principal dimensions (unit: mm); (**b**) Computational domain and meshing.

To ensure the accuracy of the numerical results and eliminate the influence of grid density, a systematic mesh independence check was performed. Four sets of meshes with different cell densities were evaluated under the operating conditions of p_p = 140 kPa and p_s = 100 kPa. The primary mass flow rate and the entrainment ratio were selected as the convergence indicators. As summarized in Table 1, the numerical solutions show a clear convergence trend as the mesh density increases. When the mesh was refined from Case C to Case D, the relative change in ER was only 0.70%. Considering both the computational accuracy and efficiency, Case C was selected as the optimal grid for all subsequent simulations.

To resolve the complex flow physics within the water-driven steam ejector, the pressure-velocity coupling was handled using the SIMPLE algorithm. To ensure numerical stability under the high-pressure

gradients and high-speed conditions, under-relaxation factors were conservatively set below 0.1. In the mixing zone, where the flow is characterized by intricate shockwave structures, the Euler-Euler framework resolves these phenomena automatically. Specifically, while standard discretization was used for most variables, a Second-Order Upwind scheme was applied to the convection terms to provide high-resolution shock-capturing capabilities. This enables the model to resolve sharp discontinuities in the pressure and density fields without the need for explicit shock-tracking algorithms. Regarding the boundary conditions, pressure-based conditions were applied at all inlets and outlets, with the secondary flow inlet specified as saturated steam at its corresponding saturation pressure. Convergence was monitored by three mass flow rates at the inlets and outlet, and the outlet water temperature; when all four parameters remained unchanged, the iteration was considered converged. Simulations were performed using a three-dimensional, steady-state, double-precision solver, requiring approximately 5×10^4 iterations per case.

Table 1: Mesh independence check.

Mesh Case	Number of Cells ($\times 10^4$)	Primary Mass Flow m_p (kg/s)	Secondary Mass Flow m_s (kg/s)	Entrainment Ratio (ER)	Relative Error of ER (%)
Case A	5.2245	0.1845	0.0028	0.0154	–
Case B	6.3356	0.1942	0.0035	0.0184	19.48%
Case C	7.0258	0.2012	0.0040	0.0199	8.59%
Case D	8.2468	0.2018	0.0040	0.0201	0.70%

2.4 Model Validation

To verify the accuracy of the numerical model, the simulation results were validated against the experimental data reported in Ref. [31]. The validation was performed under the following operating conditions: p_p = 140 kPa, T_p = 300 K, p_s = 100 kPa, and p_b = 100 kPa. As illustrated in Fig. 2, the predicted axial static pressure shows a high degree of consistency with the experimental measurements, accurately capturing the pressure drop in the suction chamber and the subsequent pressure recovery. This good agreement demonstrates that the current numerical framework is capable of reliably predicting the internal flow characteristics of the water-driven steam ejector.

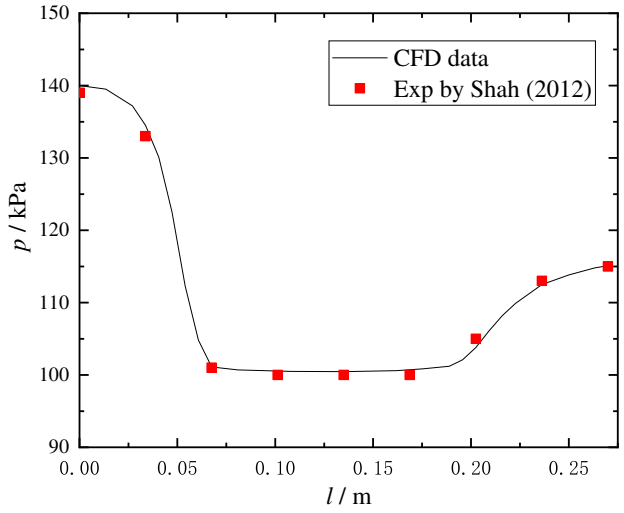

Figure 2: Comparison of axial static pressure profiles between CFD prediction and experimental data.

3 Results and Discussion

To provide a comprehensive understanding of the internal flow and thermal characteristics of the water-driven steam ejector, the following analysis focuses on the axial distributions of key parameters, including the steam plume length, pressure, temperature, and entrainment performance. The numerical simulations were conducted under varying primary-flow pressures, primary-flow temperatures, secondary-flow pressures, and outlet back pressures. The presented results highlight the influence of these operating conditions on condensation behavior, steam entrainment, and overall ejector performance.

3.1 Gas Volume Fraction and Steam Plume Length

Gas volume fraction is a key parameter for characterizing two-phase flows, as it reflects both the local phase distribution and the macroscopic flow regime within the ejector. However, obtaining reliable volume fraction data in the mixing section of a steam ejector remains challenging, especially under strong phase-change conditions. Based on the present numerical simulations, the cross-sectionally averaged volume fraction was extracted for different steam inlet pressures, and the corresponding results are presented in Fig. 3. These numerical results provide direct insight into the influence of steam inlet pressure on the evolution of phase distribution and the intensity of steam condensation in the mixing region. In this study, subscripts p, s, and b refer to the primary flow (water), the secondary flow (steam), and the outlet, respectively.

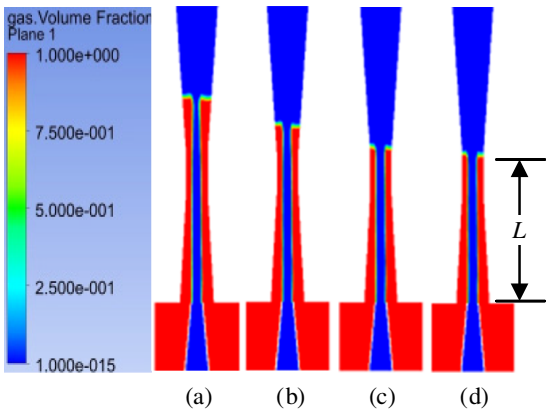

Figure 3: Contours of gas volume fraction for p_p = 139 kPa, T_p = 311.3 K at different back pressures. (**a**) p_b = 108 kPa; (**b**) p_b = 110 kPa; (**c**) p_b = 112 kPa; (**d**) p_b = 113 kPa.

Fig. 3 presents the numerically predicted gas-liquid two-phase distribution inside the ejector. It can be observed that, after being discharged from the primary nozzle, the high-pressure water jet maintains a columnar shape with nearly the same diameter as that at the nozzle exit. Owing to the shear interaction between the primary flow and the secondary flow, as well as the low pressure at the nozzle outlet, steam is entrained into the ejector. The water jet continues to flow along the centerline of the ejector, while the steam flows in the annular region surrounding the water column. Meanwhile, steam condensation occurs at the gas–liquid interface, and the steam is completely condensed into liquid water upon reaching the diffuser section of the ejector. In this process, the entrained steam undergoes direct-contact condensation within the cold driving water, allowing for the simultaneous recovery of latent heat and the integration of condensate into the working fluid.

Fig. 3a–d illustrates the variation of the axial penetration length of the steam plume under different ejector back-pressure conditions. The distance from the nozzle exit to the axial location where the steam completely disappears inside the ejector is defined as the steam plume length, denoted as L in this study.

Fig. 4 illustrates the variation of the steam plume length L under different operating conditions. It is observed that L decreases monotonically with the increment of back pressure p_b. From a hydrodynamic perspective, an increase in p_b creates a higher adverse pressure gradient along the mixing section, which effectively pushes the internal compression waves upstream. This leads to a significant reduction in the pressure difference between the suction chamber and the mixing zone, thereby suppressing the secondary steam entrainment. As the mass flow rate of the entrained steam drops, the total latent heat that needs to be absorbed by the primary water jet decreases. Consequently, the momentum and mass exchange between the phases are completed over a shorter axial distance, resulting in a contracted steam plume. This behavior is closely linked to the pressure distribution (as shown in Fig. 5), where the elevated pressure level in the mixing section diminishes the expansion ratio of the primary jet.

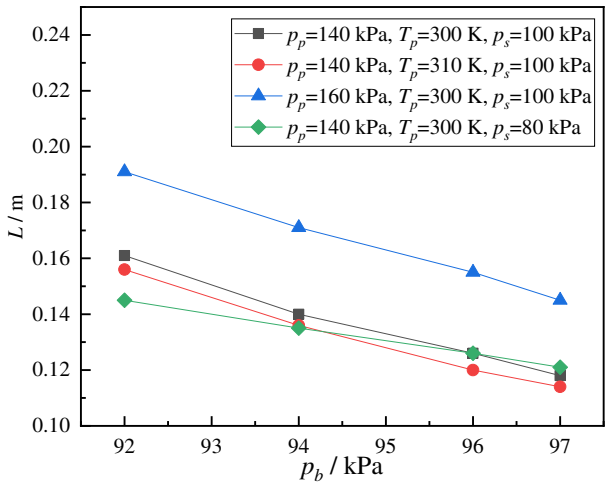

Figure 4: Effects of operating conditions on the steam plume length in the ejector.

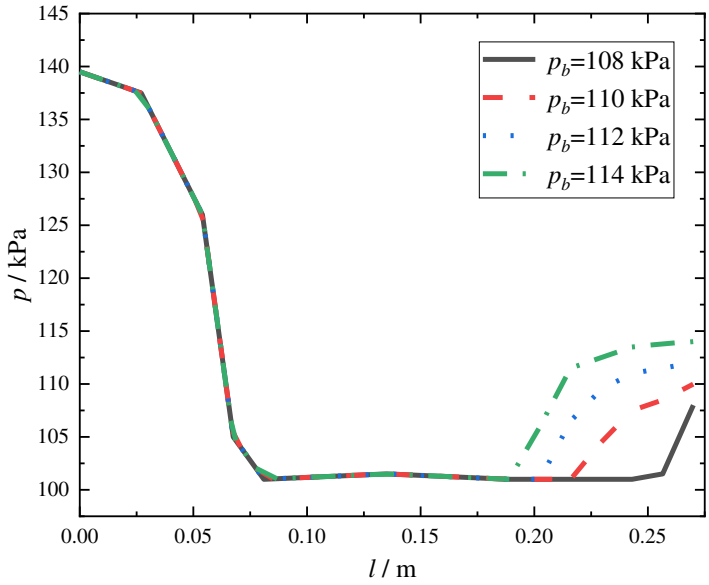

Figure 5: Variation of axial pressure at p_p = 140 kPa, T_p = 300 K, p_s = 100 kPa under different back pressures.

The sensitivity of L to inlet parameters (p_p, T_p, p_s) reveals the complex coupling between the velocity and temperature fields. Increasing the primary-stream pressure p_p results in a pronounced extension of the steam plume. This is attributed to the enhanced velocity gradient at the gas-liquid interface; the higher kinetic energy of the water jet intensifies the interfacial shear, which promotes the fragmentation of the steam phase into finer structures. However, the significantly higher axial velocity also reduces the residence time for phase change to occur at any given axial location, allowing the steam to penetrate deeper into the diffuser.

In terms of thermal driving forces, an increase in the primary water temperature T_p naturally elongates the plume. This is dictated by the reduction in subcooling degree ($DT = T_{sat} - T_p$), which serves as the fundamental potential for condensation heat transfer. As DT decreases, the local heat flux at the interface drops, requiring a larger contact area and longer contact time to achieve complete condensation. Conversely, reducing the secondary-stream pressure p_s leads to a shorter plume. Although a lower p_s might suggest a stronger suction potential, it significantly reduces the density and mass flow rate of the entrained vapor. The lower vapor-to-liquid mass ratio ensures that the primary jet's thermal capacity can quench the steam more rapidly, as evidenced by the temperature contours where the thermal equilibrium is reached much earlier in the mixing section.

3.2 The Effects of Back Pressures on Axial Pressure and Temperature Distributions

The axial pressure profile in Fig. 5 serves as a macroscopic reflection of the complex energy transformation and phase change within the ejector. The significant pressure drop within the suction chamber indicates a rapid acceleration of the entrained steam, which is consistent with the conversion of pressure energy into kinetic energy. In the initial stage of the mixing section, the pressure remains relatively stable despite the high-velocity water jet, indicating a quasi-equilibrium state where the pressure drop due to high-speed flow is partially offset by the initial steam entrainment. A critical observation is the abrupt pressure jump following the mixing section. This is not merely a gradual recovery but a condensation shock wave triggered by the rapid collapse of the steam phase. As the steam plume vanishes (correlating with Fig. 4), the sudden transition from a compressible two-phase mixture to a nearly incompressible liquid phase induces a significant volumetric contraction. This contraction, coupled with the conservation of momentum, forces a sharp conversion of kinetic energy into static pressure. The coincidence between the steam plume's disappearance and the pressure jump confirms that the completion of DCC is the primary driver for this localized pressure surge.

The sensitivity of the pressure rise location to back pressure p_b reveals the dynamic balance between the momentum flux of the primary jet and the downstream resistance. As p_b increases, the pressure rise point shifts upstream toward the mixing throat. This migration is fundamentally governed by the pressure gradient requirement for flow stabilization. Under higher back pressure, the adverse pressure gradient imposed from the exit strengthens, which restricts the expansion of the water jet and reduces its suction capacity. This leads to a higher interfacial pressure at the nozzle exit, enhancing the temperature difference between the steam and the water surface, thereby intensifying the phase transition rate per unit length. Consequently, the steam reaches its condensation limit over a shorter axial distance. The upstream shift of the shock wave suggests that the ejector's "effective mixing length" is self-adjusting; however, if the back pressure exceeds a critical threshold, the shock wave may be pushed into the nozzle area, leading to a breakdown of the entrainment performance.

As illustrated in Fig. 6, the axial temperature profile reveals the spatial evolution of the phase change intensity within the mixing section. From the primary nozzle exit to the throat, a steep temperature gradient is observed, representing the rapid dissipation of latent heat into the subcooled water jet. This process is

governed by the high interfacial heat transfer coefficient characteristic of DCC. The temperature rise is not merely a linear increase but reflects the volumetric heat source generated by the collapsing steam bubbles.

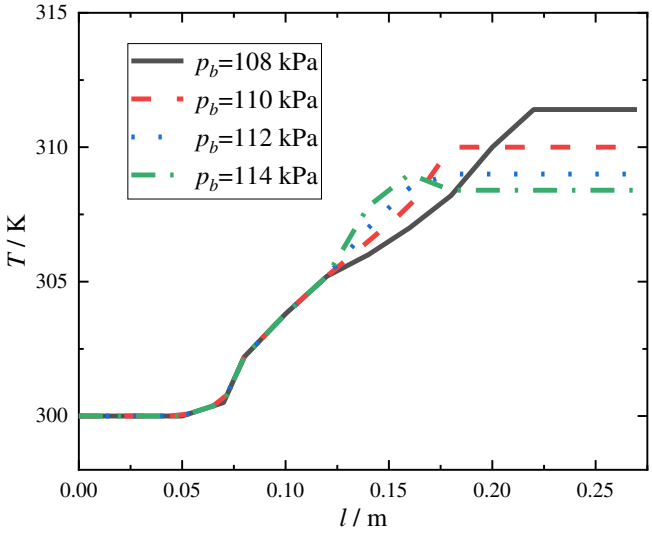

Figure 6: Variation of axial temperature at p_p = 140 kPa, T_p = 300 K, p_s = 100 kPa under different back pressures.

As the flow approaches the throat, the rate of temperature increase diminishes, asymptotically reaching a plateau. This indicates that the two-phase mixture has attained a quasi-thermal equilibrium state, where the entrained steam has been fully condensed and its latent heat has been uniformly redistributed within the liquid phase. The nearly uniform temperature distribution in the diffuser section further confirms the completion of the thermal mixing process, marking the transition from a non-equilibrium two-phase flow to a single-phase liquid flow.

The back pressure p_b significantly modulates this thermal behavior by altering the ER. A decrease in p_b enhances the pressure drop across the primary nozzle, thereby increasing the suction capacity for the secondary steam. This higher steam-to-water mass ratio increases the total thermal load per unit mass of the primary jet. Consequently, the temperature along the ejector axis rises more aggressively and reaches a higher equilibrium value. Furthermore, the lower p_b shifts the condensation front upstream, as the increased velocity difference at the nozzle exit enhances the interfacial turbulence, thereby accelerating the heat and mass transfer rates in the initial stage of the mixing section.

3.3 The Effects of Operating Conditions on the ER and the Temperature Rise Capability

The ejector performance is evaluated by the ER, defined as the ratio of the secondary mass flow rate to primary mass flow rate in Eq. (12),

$$ER = \frac{\dot{m}_s}{\dot{m}_p}. \tag{15}$$

Fig. 7 illustrates the variation of ER under different operating conditions, showing that the ER values range between 1.0% and 2.0%, which is typical for liquid-driven steam ejectors. This is attributed to the significant density disparity between the two phases; although the mass fraction of steam is small, its volumetric contribution is substantial, dominating the momentum exchange process. The results show that as the back pressure p_b increases, the ER decreases monotonically. This deterioration in entrainment capability

occurs because a higher p_b compresses the mixing zone and reduces the pressure gradient available to accelerate the secondary steam. This trend provides a macroscopic explanation for the variation in steam plume length observed in Fig. 4: a reduced ER means less steam is entrained, requiring a smaller interfacial area and shorter axial distance for complete condensation. Regarding the primary flow conditions, increasing the primary-flow pressure p_p from 140 to 160 kPa leads to an enhancement in ER. This is because the higher momentum of the water jet creates a deeper vacuum in the suction chamber, effectively drawing in more steam.

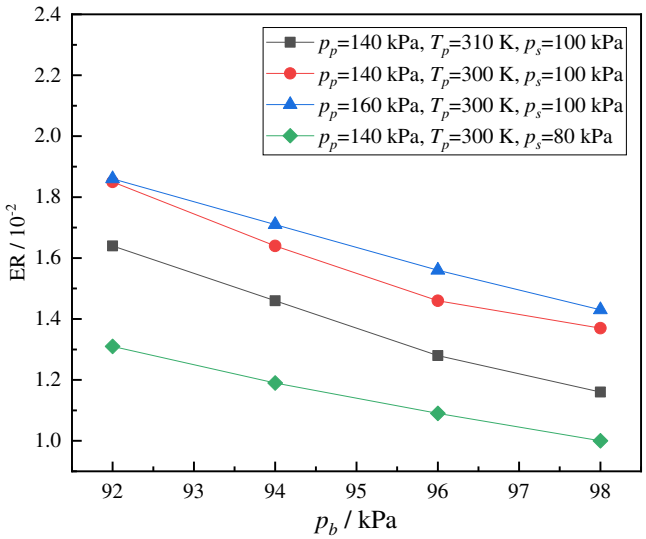

Figure 7: ER under different operating conditions.

Fig. 8 illustrates the temperature increment DT of the driving water. Within the investigated operating range, DT fluctuates between 5.33 and 11.49 K. This heating effect is primarily governed by the DCC of the entrained steam. From a thermodynamic perspective, the energy gained by the primary water flow can be approximated by the latent heat release. Consequently, the temperature rise is theoretically proportional to the ER, which explains the high degree of consistency between Figs. 7 and 8. Further analysis reveals that at higher back pressures p_b, the reduction in steam suction capacity directly limits the total enthalpy shock to the liquid phase, leading to the observed decline in DT. Interestingly, the maximum temperature rise (11.49 K) occurs at p_p = 140 kPa, T_p = 310 K, p_s = 100 kPa, p_b = 92 kPa, suggesting that under these conditions, the momentum exchange and thermal mixing reach an optimal synergy. Compared to traditional surface heat exchangers, this DCC process demonstrates a much higher heat transfer intensity, with the condensate being instantaneously integrated into the driving loop, thus eliminating the thermal resistance of a solid wall.

3.4 The Condensation Rate at Steam-Water Interface

As illustrated in Fig. 9, the contours of the condensation rate at the steam-water interface under different back pressures reveal a clear and systematic variation inside the steam-water ejector. At lower back pressures, a larger amount of steam is entrained into the mixing section, resulting in an extended region of intense condensation along the gas-liquid interface. Accordingly, high condensation rates are distributed over a longer axial distance, indicating that the DCC process persists further downstream. As the back pressure increases, the entrained steam mass flow rate decreases, and the condensation region becomes progressively compressed in the axial direction. The peak condensation rate shifts upstream and the overall condensation zone shortens, reflecting the reduced amount of steam requiring condensation.

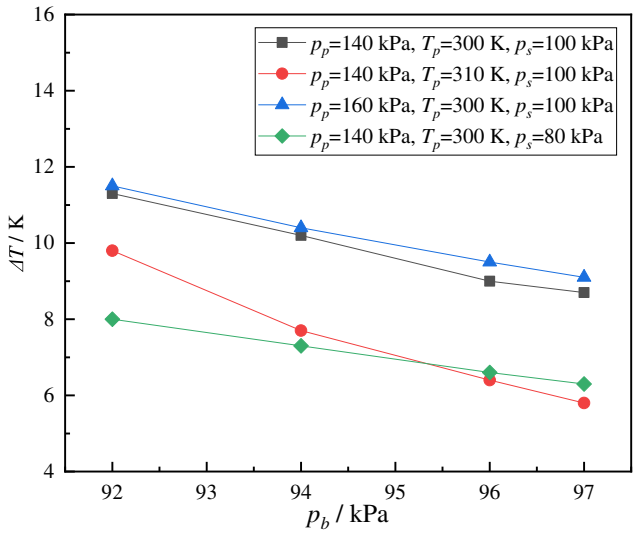

Figure 8: Temperature rise capability under different operating conditions.

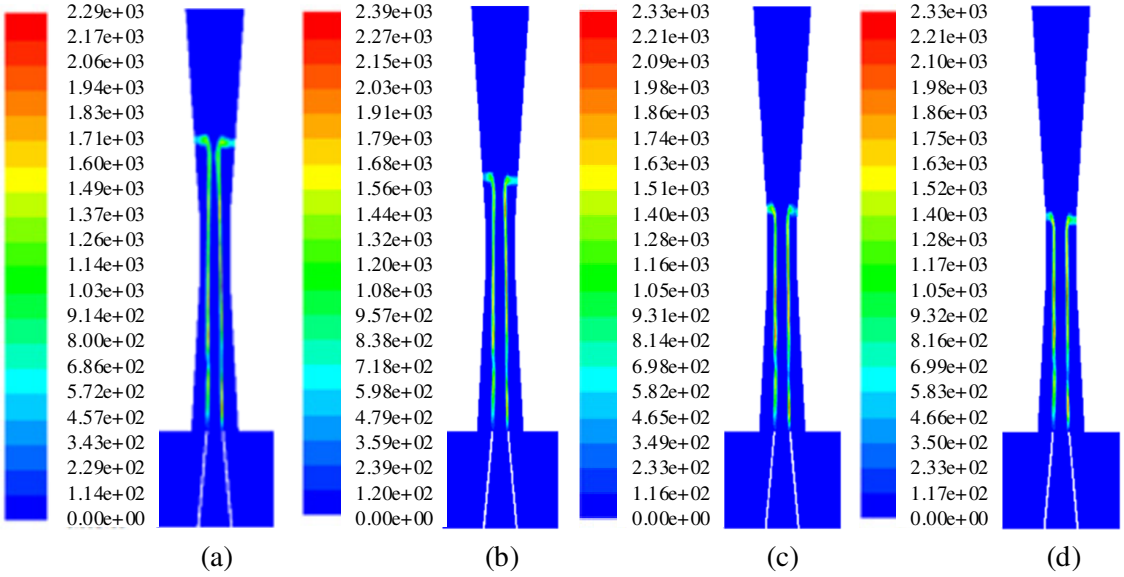

Figure 9: Contours of the condensation rate at the steam-water interface at p_p = 139 kPa, T_p = 311.3 K under different back pressures. (**a**) p_b = 108 kPa; (**b**) p_b = 110 kPa; (**c**) p_b = 112 kPa; (**d**) p_b = 113 kPa.

This trend is in good agreement with the gas volume fraction contours shown in Fig. 3. Under higher back pressure conditions, the steam core diminishes more rapidly and the steam plume disappears earlier, which corresponds to the upstream contraction of the high-condensation-rate region observed in the condensation-rate contours. Furthermore, the axial location where the condensation rate approaches zero coincides well with the position of the pressure rise shown in Fig. 5. This correspondence indicates that the completion of steam condensation is closely associated with the pressure jump in the ejector, confirming that the thermodynamic, phase-change, and pressure-recovery processes are strongly coupled.

4 Conclusions

In this study, a steam-water ejector driven by liquid water was numerically investigated using an Euler-Euler two-fluid framework coupled with a thermal-equilibrium-based DCC model. The distributions of flow, thermal, and phase-change characteristics inside the ejector were analyzed in detail. The main conclusions can be summarized as follows:

(1) The steam plume length increases with increasing primary-flow pressure, while it decreases with increasing primary-flow temperature, decreasing secondary-flow pressure, and increasing back pressure, indicating that elevated back pressure suppresses steam entrainment and shortens the condensation length.

(2) The pressure in the mixing chamber remains nearly constant, whereas a distinct pressure jump occurs at the throat, where the entrained steam is completely condensed, followed by rapid pressure recovery in the diffuser.

(3) The ER and the temperature rise slightly increase with increasing primary-flow pressure but decrease with increasing primary-flow temperature and decreasing secondary-flow pressure. An increase in back pressure leads to a continuous reduction in the ER, and flow reversal occurs when the back pressure exceeds a critical value.

(4) Back pressure strongly governs condensation behavior: increasing back pressure reduces entrained steam, shifts peak condensation upstream, shortens the condensation zone, and tightly couples condensation completion with pressure recovery.

Acknowledgement: This work was supported by the Taishan Industrial Leading Talents Program.

Funding Statement: The authors received no specific funding for this study.

Author Contributions: Conceptualization, Xianbing Chen; methodology, Xianbing Chen; software, Da Fang; validation, Chenxiao Chu; investigation, Xinhou Liu; resources, Mengyu Zhu; data curation, Da Fang; writing—original draft preparation, Da Fang; writing—review and editing, Da Fang; supervision, Xianbing Chen; project administration, Chenxiao Chu, Jinliang Zhu. All authors reviewed and approved the final version of the manuscript.

Availability of Data and Materials: Data available on request from the authors. The data that support the findings of this study are available from the Corresponding Author, [Xianbing Chen], upon reasonable request.

Ethics Approval: Ethical approval was not required for this study, as it did not involve human participants or animal subjects. All analyses were conducted using numerical simulations based on established physical models and publicly available thermophysical correlations. Therefore, ethical approval, consent to participate, and registration or approval reference numbers are not applicable.

Conflicts of Interest: The authors declare no conflicts of interest.

Nomenclatures

A	Heat transfer area
d	Bubble diameter
F	External body force
F_{lift}	Lift force
F_{vm}	Virtual mass force
h	Interfacial energy transfer term
H	Latent heat of vaporization
l	Axial position along the ejector
L	Steam plume length

m	Interfacial mass transfer term
Nu	Nusselt number
p	Pressure
Pr	Prandtl number
q	Heat flux
Q	Energy source term
R	Interfacial momentum transfer term
Re	Reynolds number
S	Mass source term
T	Temperature
v	Velocity
V	Total volume

Subscript

b	Back flow
p	Primary flow
s	Secondary flow
w	Water
v	Steam

Greek symbols

φ	Volume fraction
ρ	Density
τ	Shear stress

Abbreviations

DCC	Direct contact condensation
ER	Entrainment ratio

References

1. Zhang G, Yang H, Zuo Q, Chen J, Jin Z, Dykas S. Preliminary proposal a novel structure based on a blend condensation model to improve performance of steam ejectors in solar-driven refrigeration system. Int J Therm Sci. 2025;218(9):110168. doi:10.1016/j.ijthermalsci.2025.110168.
2. Tang Y, Zhong Z, Liu Z, Lu L, Huang Y, Wen C. Study on evolution law of non-equilibrium phase transition flow and performance improvement of steam ejector for MED-TVC desalination system. Energy. 2025;316(9):134462. doi:10.1016/j.energy.2025.134462.
3. Fergani Z, Triki Z, Menasri R, Tahraoui H, Zamouche M, Kebir M, et al. Optimizing sustainability: exergoenvironmental analysis of a multi-effect distillation with thermal vapor compression system for seawater desalination. Front Heat Mass Transf. 2024;22(2):455–73. doi:10.32604/fhmt.2024.050332.
4. Yan J, Wu X, Chong D, Liu J. Experimental research on performance of supersonic steam-driven jet injector and pressure of supersonic steam jet in water. Heat Transf Eng. 2011;32(11–12):988–95. doi:10.1080/01457632.2011.556465.
5. Yan JJ, Shao SF, Liu JP, Zhang Z. Experiment and analysis on performance of steam-driven jet injector for district-heating system. Appl Therm Eng. 2005;25(8–9):1153–67. doi:10.1016/j.applthermaleng.2004.09.001.
6. Jing H, Yuan Z, Gao J, Chen W, Chong D. Prediction of adjustable steam ejectors performance through Integration of numerical simulation and theoretical model. Appl Therm Eng. 2025;267:125841. doi:10.1016/j.applthermaleng.2025.125841.
7. Zhang G, Zuo Q, Yang Y, Jin Z, Dykas S. Numerical study on the effect of heterogeneous condensation in the primary nozzle on condensation flow and performance of steam ejector. Energy. 2025;341:139486. doi:10.1016/j.energy.2025.139486.

8. Sriveerakul T, Aphornratana S, Chunnanond K. Performance prediction of steam ejector using computational fluid dynamics: part 1. Validation of the CFD results. Int J Therm Sci. 2007;46(8):812–22. doi:10.1016/j.ijthermalsci.2006.10.014.
9. Zhang Z, Chong D, Yan J. Modeling and experimental investigation on water-driven steam injector for waste heat recovery. Appl Therm Eng. 2012;40:189–97. doi:10.1016/j.applthermaleng.2012.02.006.
10. Abe Y, Shibayama S. Study on the characteristics of the supersonic steam injector. Nucl Eng Des. 2014;268:191–202. doi:10.1016/j.nucengdes.2013.04.045.
11. Yan J, Chong D, Wu X. Effect of swirling vanes on performance of steam–water jet injector. Appl Therm Eng. 2010;30(6–7):623–30. doi:10.1016/j.applthermaleng.2009.11.007.
12. Sriveerakul T, Aphornratana S, Chunnanond K. Performance prediction of steam ejector using computational fluid dynamics: part 2. Flow structure of a steam ejector influenced by operating pressures and geometries. Int J Therm Sci. 2007;46(8):823–33. doi:10.1016/j.ijthermalsci.2006.10.012.
13. Miwa S, Endo H, Moribe T, Sakashita H, Mori M, Hibiki T. Investigation of the thermal-hydraulic characteristics of supersonic steam injector. Appl Therm Eng. 2016;109:261–71. doi:10.1016/j.applthermaleng.2016.08.069.
14. Chen X, Zhou T, Zhang W, Feng Y, Wang K, Liu H. Numerical simulation on the effect of non-condensable gas on direct contact condensation of steam jet in a narrow pipe. Int Commun Heat Mass Transf. 2024;152(3):107328. doi:10.1016/j.icheatmasstransfer.2024.107328.
15. Zhou D, Zhang Y, Zhang Y, Wu Y, Zhang G. Numerical study on the interface characteristics of gas–liquid falling film flow considering the interface forces. Phys Fluids. 2024;36(5):052108. doi:10.1063/5.0203373.
16. Eames IW, Aphornratana S, Haider H. A theoretical and experimental study of a small-scale steam jet refrigerator. Int J Refrig. 1995;18(6):378–86. doi:10.1016/0140-7007(95)98160-M.
17. Lei Y, Li S, Lu J, Xu Y, Yong Y, Xing D. Numerical analysis of steam ejector performance with non-equilibrium condensation for refrigeration applications. Buildings. 2023;13(7):1672. doi:10.3390/buildings13071672.
18. Sharifi N. Numerical study of non-equilibrium condensing supersonic steam flow in a jet-pump based on supersaturation theory. Int J Mech Sci. 2020;165(6):105221. doi:10.1016/j.ijmecsci.2019.105221.
19. Gulawani SS, Joshi JB, Shah MS, RamaPrasad CS, Shukla DS. CFD analysis of flow pattern and heat transfer in direct contact steam condensation. Chem Eng Sci. 2006;61(16):5204–20. doi:10.1016/j.ces.2006.03.032.
20. Shah A, Chughtai IR, Inayat MH. Experimental and numerical analysis of steam jet pump. Int J Multiph Flow. 2011;37(10):1305–14. doi:10.1016/j.ijmultiphaseflow.2011.07.008.
21. Zhou L, Chen W, Chong D, Liu J, Yan J. Numerical investigation on flow characteristic of supersonic steam jet condensed into a water pool. Int J Heat Mass Transf. 2017;108(12):351–61. doi:10.1016/j.ijheatmasstransfer.2016.12.013.
22. Pham TQD, Choi S. Numerical analysis of direct contact condensation-induced water hammering effect using OpenFOAM in realistic steam pipes. Int J Heat Mass Transf. 2021;171(1):121099. doi:10.1016/j.ijheatmasstransfer.2021.121099.
23. Patel S, Guleria SD, Pati A, Kumar P. Experimental analysis of direct contact condensation during vertical injection of steam onto a subcooled water pool. Phys Fluids. 2022;34(12):122111. doi:10.1063/5.0127655.
24. Zhang Y, Qu X, Zhang G, Leng X, Tian M. Effect of non-condensable gas on the performance of steam-water ejector in a trigeneration system for hydrogen production: an experimental and numerical study. Int J Hydrogen Energy. 2020;45(39):20266–81. doi:10.1016/j.ijhydene.2019.09.243.
25. Xu Q, Liang L, She Y, Xie X, Guo L. Numerical investigation on thermal hydraulic characteristics of steam jet condensation in subcooled water flow in pipes. Int J Heat Mass Transf. 2022;184(10):122277. doi:10.1016/j.ijheatmasstransfer.2021.122277.
26. Ke H, Xiao Q, Long C, Liu J, Shi L, Tang L. A modified calculation method for a centered water nozzle steam-water injector. Energies. 2022;15(23):9159. doi:10.3390/en15239159.
27. Zhou Y, Ni Y, Cui Q, Yang X, Liu J, Wei J. A novel high performance flat-evaporator loop heat pipe coupled with dual micro vapor-driven jet injectors. Energy. 2025;332(5):137285. doi:10.1016/j.energy.2025.137285.
28. Anglart H, Nylund O. CFD application to prediction of void distribution in two-phase bubbly flows in rod bundles. Nucl Eng Des. 1996;163(1–2):81–98. doi:10.1016/0029-5493(95)01160-9.

29. Hughmark GA. Mass and heat transfer from rigid spheres. AlChE J. 1967;13(6):1219–21. doi:10.1002/aic.690130638.
30. ANSYS Inc. ANSYS® academic research, release 15.0, help system, ANSYS CFX-solver theory guide. Canonsburg, PA, USA: ANSYS Inc.; 2013.
31. Shah A. Thermal hydraulic analysis of steam jet pump [dissertation]. Islamabad, Pakistan: Pakistan Institute of Engineering and Applied Sciences; 2012.